Journal of Materials Chemistry A

ROYAL SOCIETY OF CHEMISTRY

PAPER

View Article Online
View Journal | View Issue

Cite this: J. Mater. Chem. A, 2025, 13, 42187

Enhancing photothermal conversion of spinel zinc cobalt oxide through lattice distortion regulation

Huilan Ma,†[ab] Shengyang Wang,†[ab] Qi Ye,[ab] Xiaoping Tao[c] and Can Li*[ab]

Spinel oxides, renowned for their structural versatility, are used in various solar photothermal-related applications. However, the relationship between the crystal microstructure and the photothermal conversion is unknown. $ZnCo_2O_4$, a normal spinel with Co at octahedral sites, provides a model to study the link between octahedral distortion and photothermal conversion. We found that greater Jahn–Teller distortion enhances photothermal conversion efficiency (63.4% → 80.2%). Magnetic and DFT analyses attribute this improvement to a distortion-driven transition of $ZnCo_2O_4$ from a low-spin semiconductor to a high-spin metallic-like state, which promotes light-to-heat conversion. Tuning electronic behavior *via* microstructural distortion offers valuable insights for developing efficient photothermal conversion materials.

Received 19th September 2025
Accepted 3rd November 2025

DOI: 10.1039/d5ta07675g

rsc.li/materials-a

Introduction

Solar energy resources have attracted people's attention due to their clean and abundant characteristics. The capture and storage of solar energy is critical. One approach to achieve this is photothermal conversion, one of the most fundamental processes in nature. The solar to heat conversion process can cover a variety of applications, including drying and water evaporation at low temperatures, catalytic reactions, and power generation at high temperatures. No matter what the application is, its common core component is the photothermal conversion material.[1] Therefore, it is imperative to develop materials with higher photothermal conversion efficiency to achieve clean and sustainable energy infrastructure goals.

Significant efforts have been devoted to enhancing solar-to-heat performance by increasing solar absorption and minimizing thermal losses. In this context, the development of high-efficiency, cost-effective photothermal materials remains a primary focus. Most of the research in recent years has focused on designing highly absorbent materials.[2–4] So far, plenty of photothermal materials have been developed, including carbon-based materials[5] and narrow-bandgap semiconductors.[6] Among a large number of materials, spinels have been extensively investigated for solar absorbers due to their structural stability and diversity.[7–9]

Structural and compositional design is known to critically affect photothermal performance. Microstructural tuning of cobalt-based hybrid nanoreactors can couple solar evaporation with catalytic processes,[10] hierarchical MXene composites achieve ultrahigh conversion efficiencies *via* interfacial optimization, and bioinspired porous architecture enhances thermal localization and water transport.[11,12] Reviews further highlight the role of material composition and structural design in governing light-to-heat efficiency, supporting strategies based on microstructural distortion and electronic tuning.[13]

The general chemical formula of spinel materials is AB_2X_4, crystallizing in the $Fd\bar{3}m$ space group. A-site cations occupy the tetrahedrally coordinated 8a sites, while B-site cations occupy octahedrally coordinated 16d sites. Jahn–Teller (JT) active oxides have been extensively studied for their magnetic, electronic, and catalytic properties. For instance, JT distortion in $LiMn_2O_4$ influences cation ordering and magnetic coupling,[14] while cooperative JT distortion in $LaMnO_3$ drives an insulator–metal transition *via* spin-state reconfiguration.[15] Theoretical studies also suggest that JT-active ions in spinel lattices can reduce the band gap and modulate carrier transport.[16] However, the impact of JT distortion on photothermal conversion remains largely unexplored.

Variation in the occupancy of these sites by different metal ions alters the electronic structure, thereby affecting the photothermal conversion process. In particular, the d orbitals play an important role in the photoexcitation observed, which has been used in developing photocatalysts capable of using the less energetic but more abundant visible light.[17–19] There are some transition metal ions that can introduce lattice distortion in the octahedral site in spinels.[20,21] Although well known, its effect on photothermal conversion efficiency has often been overlooked. Efficient conversion requires both broadband solar absorption

[a]State Key Laboratory of Catalysis, Dalian Institute of Chemical Physics, Chinese Academy of Sciences, Dalian National Laboratory for Clean Energy, Dalian 116023, China

[b]University of Chinese Academy of Sciences, Beijing 100049, China. E-mail: canli@dicp.ac.cn

[c]Chongqing University, Chongqing 401331, China

† Contributed equally to the manuscript.

and adequate electron–phonon transport. Most previous efforts have focused on tuning the electronic structure of the material to enhance solar absorption and photothermal conversion efficiency.[22,23]

$ZnCo_2O_4$ is a representative normal spinel oxide, where the tetrahedral sites (Td) are only occupied by Zn^{2+} while Co^{3+} occupies the Oh sites. In this regard, $ZnCo_2O_4$ is an ideal model to understand the relationship between the microstructure and photothermal performance. In this work, we demonstrate that the photothermal conversion efficiency of a spinel is highly dependent on the degree of the lattice distortion in CoO_6 octahedra. Analyses *via* XRD, SQUID, and DFT indicate that lattice distortion strongly enhances photothermal conversion. Distortion of CoO_6 octahedra triggers a semiconductor-to-metal transition, promoting charge recombination and efficient light-to-heat conversion. The most distorted sample (ZCO-300 °C) achieves the highest light absorption and photothermal conversion efficiency, demonstrating that tuning octahedral distortion is a key strategy to optimize photothermal performance.

Results and discussion

Morphology and structure characterization of samples

A simple sol–gel method was adopted to prepare the $ZnCo_2O_4$ precursor. Then the obtained precursor was calcined at different temperatures. XRD patterns of ZCO-300 °C, ZCO-400 °C, ZCO-500 °C, and ZCO-600 °C samples are shown in Fig. 1a, and the diffraction peaks are consistent with the standard PDF card of $ZnCo_2O_4$ (JCPDS no. 23-1390). The diffraction peaks of calcined samples shift to a higher angle as the calcination temperatures increase, indicating the presence of lattice contraction in these samples.[24] Fig. 1b shows the Raman spectroscopy results, which further confirm the above assignments. The characteristic vibration peaks at ~182 cm^{-1}, ~477 cm^{-1}, ~515 cm^{-1}, and ~613 cm^{-1} are assigned to the strong vibration modes F2g, Eg, F2g and F2g respectively. The Raman vibrational mode (*i.e.*, A1g) results in a peak positioned at 686 cm^{-1} consistent with the previous studies of $ZnCo_2O_4$ spinel.[25] As the synthesis temperature increases from 300 °C to 600 °C, the Raman peaks become sharper and more intense, suggesting enhanced crystallinity. A slight redshift and broadening of the A_1g mode are observed at 300 °C, indicative of local lattice distortion related to Jahn–Teller active Co^{3+} ions in octahedral coordination. Fig. 1c–f shows the scanning electron microscopy (SEM) images of $ZnCo_2O_4$, which indicate that both spinel oxides are aggregated nanoparticles without apparent difference.

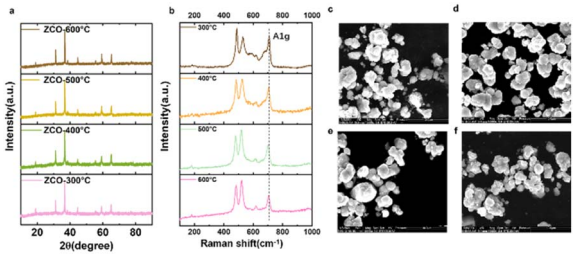

Fig. 1 Structure characterization of ZCO-300 °C, ZCO-400 °C, ZCO-500 °C and ZCO-600 °C. (a) XRD patterns and (b) Raman spectra of $ZnCo_2O_4$ at different calcination temperatures. TEM patterns of (c) ZCO-300 °C, (d) ZCO-400 °C, (e) ZCO-500 °C and (f) ZCO-600 °C.

CoO_6 octahedral Jahn–Teller distortion of samples

To investigate the structural evolution and CoO_6 octahedral distortion of the spinel $ZnCo_2O_4$, we employed the Rietveld refinement method to analyze the XRD data (Fig. 2a–d). Refinement results reveal that all synthesized samples are in a single phase with the *Fd*-$\bar{3}$*m* space group (cubic, 227). As we know, the spinel oxides are enriched with octahedral sites and are likely to undergo Jahn–Teller distortion to eliminate the orbital degeneracy to maintain the energy stability of the system. As illustrated in Fig. 2e, the distance of Co–O bonds at the octahedral sites is gradually decreased, accompanied by the increase of calcination temperatures, which demonstrates that a compressive strain exists in the calcined samples. Additionally, the cell volume of the samples shows a decrease because the heating treatment contributes to the crystallite process of $ZnCo_2O_4$ spinel (Tables S1 and S2). We used the formula[20] to calculate the distortion of the octahedral sites and found that as the calcination temperature decreases, the degree of distortion gradually increases (Fig. 2f). These results confirm that the Jahn–Teller distortion modulates the local bonding

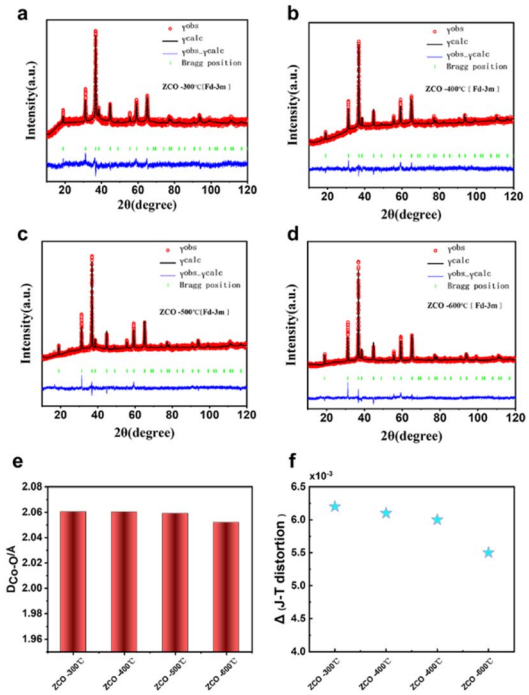

Fig. 2 XRD refined patterns of ZCO-300 °C, ZC0-400 °C, ZCO-500 °C and ZCO-600 °C: (a) ZCO-300 °C, (b) ZCO-400 °C, (c) ZCO-500 °C and (d) ZCO-600 °C. (e) Length of the Co–O bond in $ZnCo_2O_4$ at different calcination temperatures. (f) J–T distortion of $ZnCo_2O_4$ at different calcination temperatures.

environment, consistent with the proposed distortion-driven mechanism in Raman analysis.

$$\Delta = \frac{1}{6}\sum \frac{(R_i - R_{av})^2}{R_{av}^2} \quad (1)$$

Analysis of the magnetic properties of the samples

The elongation or compression of the Co–O bond along the *z*-axis direction can significantly affect the electron configuration of the t_{2g} and e_g orbitals, thus exerting a great effect on the spin state of Co^{3+} ions.[26] The magnetic properties and the related spin information of the as-synthesized $ZnCo_2O_4$ were thereafter used for the detection of the extremely subtle magnetic field. Fig. 3a shows the recorded magnetization curves in a magnetic field from 0 to 50 kOe. The magnetization curves of all the samples show similar profiles and no hysteresis feature shows up, suggesting paramagnetic behaviors under ambient conditions.[27]

The change in magnetic susceptibility was characterized by the Superconducting Quantum Design (SQUID) technique.[28] The magnetic moment evolution measured by the SQUID magnetometer clearly verifies the expected trend of spin-state modulation in the samples.

Further temperature-dependent magnetization characterization was carried out using field-cooling procedures at H = 1000 Oe in the range of 2 to 300 K (Fig. 3b). In the high temperature domain (above 150 K), the susceptibilities derived from the magnetizations obey a paramagnetic Curie–Weiss law:

$$\chi = \frac{M}{H} \quad (2)$$

$$\chi = \chi_0 + \frac{C}{T - T_C} \quad (3)$$

where χ_0 is the temperature-independent contribution, and C and T_C are the Curie constant and Curie–Weiss temperature, respectively.[29] The fitting results for the samples are shown in Fig. S1. Based on the fitting results the effective magnetic moment μ_{eff} can be acquired through $\mu_{eff} = \sqrt{(8C)}\mu_B$ (Fig. 3c). As the calcined treatment increases, the μ_{eff} decreases, more details are provided in Table S3. For octahedrally coordinated Co^{3+}, most of the recent experimental and theoretical studies highlight that the mixture of LS and HS states is more reasonable.[29,30] Therefore, we treated the spin state of Co^{3+} as a mixture of HS state (4.9 μ_B) and LS state (0 μ_B) in this work. Using these values, the volume fractions of Co^{3+} in HS and LS states can be calculated as shown in Fig. 3d. More details are presented in Table S3. ZCO-300 °C has the highest content of HS Co^{3+} ions compared to other calcined samples. In detail, the HS and LS fractions in the ZCO-300 °C sample are 34% and 66%, respectively. The contributions of the HS state in the samples after heat treatment gradually decrease with increase in temperature.

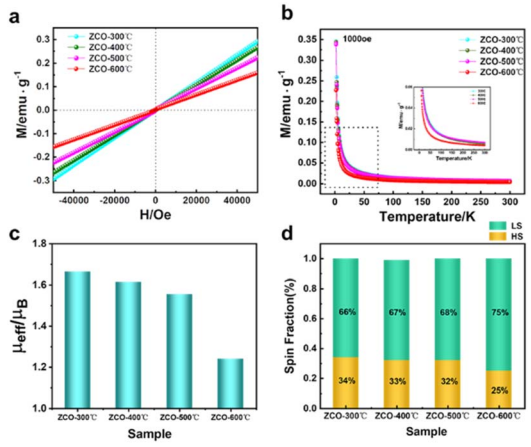

Fig. 3 Magnetic properties of ZCO-300 °C, ZCO-400 °C, ZCO-500 °C and ZCO-600 °C samples. (a) Hysteresis loops of the as-prepared spinel $ZnCo_2O_4$ samples recorded at room temperature (300 K). (b) Temperature-dependent magnetization characterization of the as-prepared samples at H = 1000 Oe. (c) Effective magnetic moment of samples. (d) High- and low-spin state fractions of each sample.

DFT + U calculations of samples

$ZnCo_2O_4$ is a normal spinel with Zn^{2+} and Co^{3+} residing in the four-coordinated tetrahedral and six-coordinated octahedral sites, respectively (Fig. 4a). Because of the high crystal field splitting energy, Co^{3+} generally favors a low-spin (LS) state (t_{2g}^6 e_g^0) in an octahedral environment,[31] where the t_{2g} orbitals are fully occupied and e_g orbitals are fully empty (Fig. 4b). This gives rise to a purely localized electronic structure and therefore an intrinsic semiconductor feature.[32] The vacant e_g orbitals provide an opportunity to manipulate Co^{3+} from the low-spin to the high-spin state, which, from an electronic perspective, markedly alters the photothermal conversion process of $ZnCo_2O_4$.- The empty e_g orbitals can allow up to two unpaired electrons to reside, forming the intermediate-spin (IS) state (t_{2g}^5 e_g^1) and high-spin (HS) state (t_{2g}^4 e_g^2), respectively. In Fig. 4c, by performing density functional theory (DFT) calculations, we observed that the octahedral units underwent gradual lattice distortion (Table S4) when manually increasing the unpaired spins in $ZnCo_2O_4$. This is because the increase of the cobalt spin state forces the two originally empty e_g orbitals to be steadily occupied, which gives rise to a degenerate electronic ground state. This electronic state is unstable and induces the Jahn–

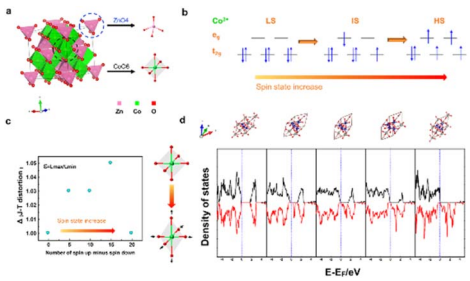

Fig. 4 DFT + U calculation of ZCO-300 °C, ZCO-400 °C, ZCO-500 °C and ZCO-600 °C samples. (a) Crystal structure of the spinel $ZnCo_2O_4$ with Zn and Co occupying the tetrahedral and octahedral sites, respectively. (b) Illustration of the Co^{3+} spin state transition from low spin to high spin. (c) J–T distortion in the octahedral site as the spin state increases. (d) Density of states (DOS) of $ZnCo_2O_4$ as the spin state increases.

Teller effect to lower the energy as well as the symmetry of the system.[33] As a result, the degeneracy is broken, and the octahedral units exhibit elongated distortion. The density of states (DOS) patterns in Fig. 4d provide a more visual illustration of the spin channel evolution during the process of cobalt spin state increase. For $ZnCo_2O_4$ with no spin manipulation, the spin-up and spin-down densities are completely symmetric, and no channel lies across the Fermi level. When the spin state of Co^{3+} is manually raised, the symmetry of DOS is gradually destroyed. Meanwhile, the electronic density starts to become continuous as a result of the delocalized electrons and eventually, a channel connecting the states below and across the Fermi level appears and propagates. Note that the channel is strictly propagated in the spin-up domain, suggesting that distortion-selected charge transport is induced and promoted.[34] At the same time, due to the lattice distortion in the CoO_6 octahedral site in $ZnCo_2O_4$, it was found that the material's properties also changed from semiconductor to metal in an upper-limit model which contributes to the absorption and the photothermal conversion process of the samples.

Photothermal conversion performance of $ZnCo_2O_4$

To understand the relationship between lattice distortion and photothermal conversion, we conducted the photothermal tests of $ZnCo_2O_4$ spinel under the irradiation of a Xe lamp ($P = 4.5$ KW m^{-2}), which has an irradiation spectrum similar to solar irradiation. The greater the distortion caused, the greater the proportion of high spin, and thus the greater the absorption of the material (Fig. 5a). Specifically, the band gap of the materials was also determined from UV-vis-IR absorption spectra, showing a gradual decrease with increasing calcination temperature (Fig. S2 and Table S5), which aligns well with the DFT-calculated trend. During the tests, the surface temperature of $ZnCo_2O_4$ spinel oxides was recorded using an IR camera (Fig. 5b). The temperature of both samples rapidly increased to a stationary value. The temperature of ZCO-300 °C increased from 25.0 to 125.0 °C and reached a steady value after 120 s under irradiation, while within the same testing period, the peak temperature of ZCO-600 °C only reached 114.7 °C at the same time, both of which are stable for 6 cycles (Fig. 5c and S2). According to the thermal equilibrium calculations (Fig. S3 and Table S6), the internal photothermal efficiency of ZCO-300 °C is 80.2%, being much higher than that of ZCO-600 °C (63.4%). These results strongly indicate that the degree of distortion within the CoO_6 octahedron plays an important role in photothermal conversion, with severely distorted structures being particularly effective in promoting photo heat generation. Besides, the temperature elevation behaviors of $ZnCo_2O_4$ are highly reproducible after three on/off cycles of photothermal conversion under concentrated Xe lamp light irradiation.

The distortion of the octahedral sites causes the rearrangement of electrons, which is manifested in changes in the spin and absorption of the material. Similarly, we can verify that the calcination temperature can effectively change the degree of material distortion by observing the change in the thermal conductivity of the material with temperature. As shown in Fig. 5d, the thermal conductivity of the material changes with temperature. The thermal conductivity of the material calcined at 600 °C is higher than that of the material calcined at 300 °C. Greater lattice distortion in a crystal enhances phonon scattering and reduces the phonon mean free path, thereby lowering the thermal conductivity.[35] At the same time, as the distortion increases, the material changes from a semiconductor to a metallic state, making the energy band of the material continuous. This transition would dramatically reduce the lifetime of electrons and holes[36] which would transfer energy to the crystal lattice faster, resulting in lattice relaxation and improving the photothermal conversion efficiency of the material (Fig. 5e).

To demonstrate the practical potential of the material for photothermal applications, we performed a proof-of-concept solar evaporation test. Under one-sun illumination, the material exhibited efficient water evaporation, achieving a rate of

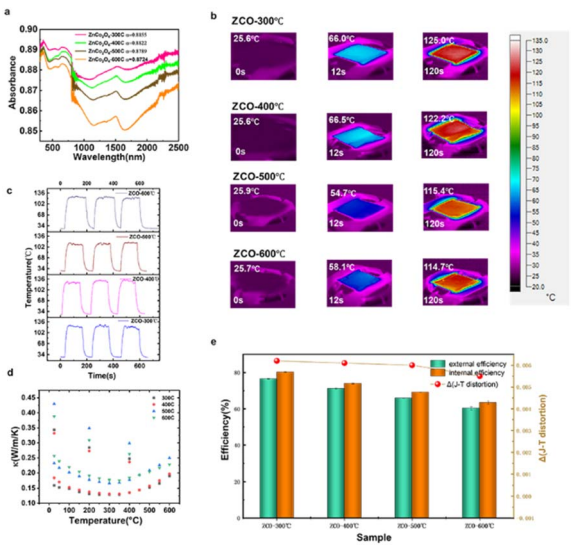

Fig. 5 Photothermal conversion test of ZCO-300, ZCO-400, ZCO-500, and ZCO-600 samples. (a) UV-vis-IR spectra of the as-prepared spinel $ZnCo_2O_4$ samples. (b) Surface temperature of samples measured by IR camera. (c) Temperature–time cycle curves of samples. (d) Thermal conductivity data of samples. (e) Summary of the relationship between photothermal conversion efficiency and lattice distortion.

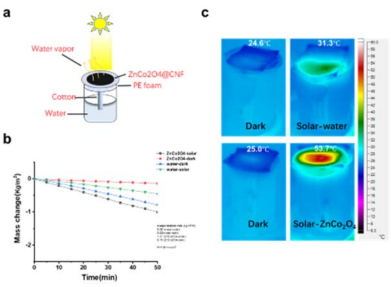

Fig. 6 Proof-of-concept demonstration of the photothermal water evaporation performance. (a) Schematic illustration of the experimental setup. (b) Surface temperature of the materials under one-sun illumination. (c) Water evaporation rates of the sample.

1.21 kg m^{-2} h^{-1} (Fig. 6). These results illustrate the material's applicability in solar-driven water evaporation and energy conversion.

Conclusions

In summary, by employing spinel $ZnCo_2O_4$ synthesized at various calcination temperatures, we have demonstrated the efficacy of lattice distortion in enhancing photothermal conversion efficiency and that XRD refinement and magnetic characterization can be employed to identify the Jahn–Teller distortion in the lattice introducing the HS state in the CoO_6 octahedral site. Also, the DFT calculations suggest that the lattice distortion will induce more IS states in the CoO_6 site. The distortion-engineered $ZnCo_2O_4$ is predicted to have more HS fraction in the CoO_6 site, which would introduce more Jahn–Teller distortion in the lattice. Subsequent experiments establish a straightforward approach to engineer lattice distortion in CoO_6. The best-performing ZCO-300 °C sample with the largest degree of lattice distortion exhibits decent photothermal conversion efficiency that outperforms other Co-based oxides. Our work emphasizes that the rationality and benefits of engineering the lattice distortion of metal oxides is an approach to advanced photothermal conversion efficiency.

Author contributions

Huilan Ma wrote the manuscript and conducted most of the experiments and DFT calculations. Shengyang Wang revised the manuscript. Xiaoping Tao characterized the SQUID magnetic data. Qi Ye was involved in the discussion of the experiment. Can Li revised the manuscript and supervised this work. All authors discussed and revised the manuscript.

Conflicts of interest

There are no conflicts to declare.

Data availability

Additional datasets generated during this study are available from the corresponding author upon reasonable request.

Supplementary information (SI): XRD patterns, magnetic characterization, photothermal conversion measurements, and DFT calculation results. See DOI: **https://doi.org/10.1039/d5ta07675g**.

Acknowledgements

This work was conducted by the Fundamental Research Center of Artificial Photosynthesis (FReCAP), financially supported by the National Natural Science Foundation of China (NSFC) under Grant No. 22088102. The authors thank Wang Chen (Dalian Institute of Chemical Physics) for his valuable assistance in magnetic data analysis.

Notes and references

1 X. Li, W. Xu, M. Tang, L. Zhou, B. Zhu, S. Zhu and J. Zhu, *Natl. Acad. Sci. U. S. A.*, 2016, **113**, 13953–13958.
2 X.-G. Zhao, D. Yang, Y. Sun, T. Li, L. Zhang, L. Yu and A. Zunger, *J. Am. Chem. Soc.*, 2017, **139**, 6718–6725.
3 L. Yang, G. Chen, N. Zhang, Y. Xu and X. Xu, *ACS Sustain. Chem. Eng.*, 2019, **7**, 19311–19320.
4 J. W. Choi, B. Shin, P. Gorai, R. L. Hoye and R. Palgrave, *ACS Energy Lett.*, 2022, **7**, 1553–1557.
5 Y. Li, T. Gao, Z. Yang, C. Chen, W. Luo, J. Song, E. Hitz, C. Jia, Y. Zhou and B. Liu, *Adv. Mater.*, 2017, **29**, 1700981.
6 J. Wang, Y. Li, L. Deng, N. Wei, Y. Weng, S. Dong, D. Qi, J. Qiu, X. Chen and T. Wu, *Adv. Mater.*, 2017, **29**, 1603730.
7 L. Kaluža, B. Orel, G. Dražič and M. Kohl, *Sol. Energy Mater. Sol. Cells*, 2001, **70**, 187–201.
8 S. Atchuta, S. Sakthivel and H. C. Barshilia, *Sol. Energy*, 2020, **199**, 453–459.
9 L. KalužA, A. Šurca-Vuk, B. Orel, G. Dražič and P. Pelicon, *J. Sol-Gel Sci. Technol.*, 2001, **20**, 61–83.
10 H. Zhu, R. Du, H. Zhao, M. Liu, Y. Wang, C. Yu, Z. Guo, S. Tang, E. H. Ang and F. Yang, *J. Mater. Chem. A*, 2024, **12**, 8487–8501.
11 M. Hu, T. Cui, Y. Wang, Y. Zheng, M. Zhang, E. H. Ang and J. Zhu, *Small*, 2025, **21**, e07152.
12 K. Shi, M. Aizudin, M. Pan and E. H. Ang, *Mater. Horiz.*, 2025, **12**, 2389–2397.
13 X. Cui, Q. Ruan, X. Zhuo, X. Xia, J. Hu, R. Fu, Y. Li, J. Wang and H. Xu, *Chem. Rev.*, 2023, **123**, 6891–6952.
14 W.-W. Liu, D. Wang, Z. Wang, J. Deng, W.-M. Lau and Y. Zhang, *Phys. Chem. Chem. Phys.*, 2017, **19**, 6481–6486.
15 I. Loa, P. Adler, A. Grzechnik, K. Syassen, U. Schwarz, M. Hanfland, G. K. Rozenberg, P. Gorodetsky and M. Pasternak, *Phys. Rev. Lett.*, 2001, **87**, 125501.
16 C. Li, P. Li, L. Li, D. Wang, X. Gao and X. J. Gao, *RSC Adv.*, 2021, **11**, 21851–21856.
17 A. L. Linsebigler, G. Lu and J. T. Yates Jr, *Chem. Rev.*, 1995, **95**, 735–758.
18 B. Geoffrey and E. Thomas, *J. Phys. Chem. B*, 1997, **101**, 2508–2513.
19 Y. I. Kim, S. Salim, M. J. Huq and T. E. Mallouk, *J. Am. Chem. Soc.*, 1991, **113**, 9561–9563.
20 X. Zhang, C. Pei, X. Chang, S. Chen, R. Liu, Z.-J. Zhao, R. Mu and J. Gong, *J. Am. Chem. Soc.*, 2020, **142**, 11540–11549.
21 E. Navickas, Y. Chen, Q. Lu, W. Wallisch, T. M. Huber, J. Bernardi, M. Stöger-Pollach, G. Friedbacher, H. Hutter and B. Yildiz, *ACS Nano*, 2017, **11**, 11475–11487.
22 M. Gao, L. Zhu, C. K. Peh and G. W. Ho, *Energy Environ. Sci.*, 2019, **12**, 841–864.
23 X. Chen, L. Liu, P. Y. Yu and S. S. Mao, *Science*, 2011, **331**, 746–750.
24 Z.-Y. Guo, Y. Si, W.-Q. Xia, F. Wang, H.-Q. Liu, C. Yang, W.-J. Zhang and W.-W. Li, *Proc. Natl. Acad. Sci. U. S. A.*, 2022, **119**, e2201607119.
25 K. Samanta, P. Bhattacharya, R. Katiyar, W. Iwamoto, P. Pagliuso and C. Rettori, *Phys. Rev. B*, 2006, **73**, 245213.

26 Y. Cao, L. Gao, Z. Lai, C. Wang, Y. Yao, X. Zhu and Z. Zou, *Appl. Phys. Lett.*, 2021, **119**, 162103.
27 T. S. Herng, D.-C. Qi, T. Berlijn, J. Yi, K. Yang, Y. Dai, Y. Feng, I. Santoso, C. Sanchez-Hanke and X. Gao, *Phys. Rev. B: Condens. Matter Mater. Phys.*, 2010, **105**, 207201.
28 R. M. Ramsundar, V. K. Pillai and P. A. Joy, *Phys. Chem. Chem. Phys.*, 2018, **20**, 29452–29461.
29 S. Zhou, X. Miao, X. Zhao, C. Ma, Y. Qiu, Z. Hu, J. Zhao, L. Shi and J. Zeng, *Nat. Commun.*, 2016, **7**, 11510.
30 M. Karolak, M. Izquierdo, S. L. Molodtsov and A. I. Lichtenstein, *Phys. Rev. Lett.*, 2015, **115**, 046401.
31 J. Goodenough and P. Raccah, *J. Appl. Phys.*, 1965, **36**, 1031–1032.
32 L. Wu, L. Sun, X. Li, Q. Zhang, H. Si, Y. Zhang, K. Wang and Y. Zhang, *Appl. Surf. Sci.*, 2020, **506**, 144964.
33 V. Gnezdilov, V. Fomin, A. Yeremenko, K.-Y. Choi, Y. Pashkevich, P. Lemmens, S. Shiryaev, G. Bychkov and S. Barilo, *J. Low Temp. Phys.*, 2006, **32**, 162–168.
34 Y. Sun, S. Sun, H. Yang, S. Xi, J. Gracia and Z. J. Xu, *Adv. Mater.*, 2020, **32**, 2003297.
35 S. Zhu, J. Zhu, S. Ye, K. Yang, M. Li, H. Wang and J. He, *J. Am. Chem. Soc.*, 2023, **106**, 6279–6291.
36 H. Huang, L. Zhang, Z. Lv, R. Long, C. Zhang, Y. Lin, K. Wei, C. Wang, L. Chen and Z.-Y. Li, *J. Am. Chem. Soc.*, 2016, **138**, 6822–6828.

